Case Studies in Thermal Engineering 24 (2021) 100860

Contents lists available at ScienceDirect

Case Studies in Thermal Engineering

journal homepage: http://www.elsevier.com/locate/csite

Computational investigation of thermal behavior and molten metal flow with moving laser heat source for selective laser melting process

Patiparn Ninpetch [a], Pruet Kowitwarangkul [a,*], Sitthipong Mahathanabodee [b], Prasert Chalermkarnnon [c], Phadungsak Rattanadecho [d]

[a] The Sirindhorn International Thai-German Graduate School of Engineering (TGGS), King Mongkut's University of Technology North Bangkok, Bangkok, Thailand
[b] Department of Production Engineering, Faculty of Engineering, King Mongkut's University of Technology North Bangkok, Bangkok, Thailand
[c] Assistive Technology and Medical Devices Research Center, National Science and Technology Development Agency, Pathum Thani, Thailand
[d] Department of Mechanical Engineering, Faculty of Engineering, Thammasat University (Rangsit Campus), Pathumthani, Thailand

GRAPHICAL ABSTRACT

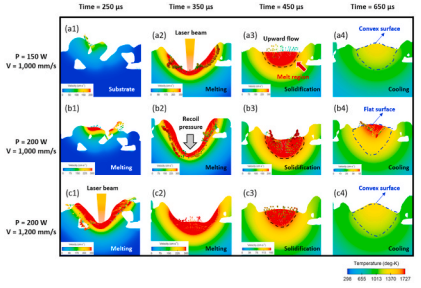

ARTICLE INFO

Keywords:
Numerical modelling
Additive manufacturing
Selective laser melting
Moving laser heat source
Molten metal flow

ABSTRACT

Selective laser melting (SLM) process, which is one type of additive manufacturing (AM) processes, involves numerous complex physical phenomena such as heat transfer, molten metal flow, phase transformation, and Marangoni effect. These phenomena have significant effect on the final products quality. The aims of this research are to investigate the thermal behavior and molten metal flow characteristics, and to analyze the influence of the process parameters on scanning track formation. An integrated numerical modelling of discrete element method (DEM) and

* Corresponding author. King Mongkut's University of Technology North Bangkok, 1518 Pracharat 1 Road, Wongsawang, Bangsue, Bangkok, 10800, Thailand.
E-mail address: pruet.k@tggs.kmutnb.ac.th (P. Kowitwarangkul).

https://doi.org/10.1016/j.csite.2021.100860
Received 8 September 2020; Received in revised form 10 January 2021; Accepted 19 January 2021
Available online 23 January 2021

computational fluid dynamics (CFD) are applied. The results reveal that the molten metal backward flowed from the laser hot spot to the rear of the melt pool due to the surface tension gradient. The uniform tear-drop shape and high penetration scanning track occurred with laser power and scanning speed of 200 W and 1000 mm/s, 250 W and 1000 mm/s, and 250 W and 1200 mm/s. Moreover, the scanning track width and depth of all scanning speed levels, 1000 mm/s, 1200 mm/s, and 1500 mm/s, increased around 4–10 μm and 14–22 μm, respectively, with the increase in laser power of 50 W and reduced around 1–4 μm and 3–6 μm, respectively, per increasing in scanning speed of 100 mm/s.

1. Introduction

Selective laser melting (SLM) process is a powder-based AM process for fabrication the metallic components with elaborate structure that uses moving laser heat source for melting the metal powder bed to achieve the full dense parts [1–3]. The advantages of SLM process include freedom in products design, low material loss, and near-net-shape parts production [4,5]. Several complex physics phenomena such as heat transfer, molten metal flow, phase transformation, and Marangoni effect which have a crucial effect on the final parts quality, can take place during SLM process [6]. These complex physical phenomena are very difficult to observe by experiment because they appear in a short period and a micro level. However, numerical modelling is an effective method that provides a better understanding of the mechanism of complex physical phenomena in SLM process [7,8]. Over recent years, the numerical models for SLM process using the finite difference method (FDM) or finite volume methods (FVM) have been developed by many researchers [9–11]. For instance, Y. Li and D. Gu [12] developed a three-dimensional model to investigate the thermal behavior of pure titanium powder in SLM process with ANSYS software. Patiparn et al. [13] investigated the influence of laser power and scanning speed on the melt pool shape of AISI 420 in SLM process by using numerical modelling method. The results of the study presented that shape of melt pools can be changed from ellipse shape to tear drop shape with an increase in scanning speed. Moreover, a three-dimensional SLM process of AIS H13 simulation was developed to examine the melt-pool behavior of a randomly-distributed powder bed with keyhole formation by Nd-YAG laser [14]. It was found that the keyhole mode, narrow and deep melt pool, can be formed when evaporation occurs.

In the current study, a powder-scaled computational fluid dynamics (CFD) model was applied to investigate the thermal behavior and molten fluid flow characteristic, and analyze the effects of process parameters, namely laser power and scanning speed on scanning track formation in SLM process. The integration of discrete element method (DEM) model and CFD model were used to generate the powder bed layer on the solid substrate and to simulate the molten metal flow characteristic. A moving Gaussian heat source model was modeled as a moving heat flux on the top of the powder bed layer. The laser power, scanning speed, layer thickness, and laser spot size used in this study were 150 W, 200 W, 250 W, 1000 mm/s, 1200 mm/s, 1500 mm/s, 50 μm, and 52 μm respectively. The result from numerical modelling was validated with the experimental study result reported by Y. Ch. Wu et al. [14].

2. Numerical modelling approach

2.1. Heat transfer and molten metal flow equations

The complex physical phenomena such as heat transfer, molten metal flow in SLM process can be solved by using CFD model, which is based on mass, energy, and momentum conservation equations [15]. Considering the phase transformation between the solid phase and liquid phase, the latent heat of fusion model was applied to simulate the phase transformation. In addition, the volume of fluid (VOF) method was used to track the melt pool surface geometry and position [16].

Marangoni effect is the phenomenon which relates to the mass transfer along the melt pool surface due to the surface tension gradient. The Marangoni effect strongly influences the surface morphology of molten pool and heat convection. The surface tension model with temperature dependence is shown in Eq. (1) [14,15].

$$\gamma\,(\mathrm{T}) = \gamma_{\mathrm{o}} + \frac{d\gamma}{\mathrm{dT}}(\mathrm{T} - \mathrm{T_m}) \tag{1}$$

where Y is the surface tension at temperature T, Y_o is the surface tension at melting (liquidus) temperature, T_m is melting temperature, and $\frac{d\gamma}{\mathrm{dT}}$ is surface tension coefficient with temperature dependence.

The materials evaporation occurs when temperature exceeds the boiling point of materials. Moreover, the melt pool morphology affected by evaporation can be determined by a recoil pressure over the molten metal surface [14,15]. The recoil pressure equation is expressed as:

$$\mathrm{P_r} = 0.54\mathrm{P_o}\exp\left(\Delta\mathrm{H_v}\frac{\mathrm{T} - \mathrm{T_b}}{\mathrm{RTT_b}}\right) \tag{2}$$

where ΔH_v is the enthalpy of metal vapor, P_o is the saturation pressure, R is gas constant, and T_b is boiling temperature of material.

The Gaussian heat source model was defined to simulate the laser moving heat source that takes place on the top of the powder bed layer which can be expressed as Eq. (3) [15].

$$Q = \frac{2A_b P_L}{\pi \Phi_e} \exp\left(-2\frac{(x - x_s)^2 + (y - y_s)^2}{\Phi_e^2} \right) \quad (3)$$

where Q is the instant surface heat flux, A_b is the absorption coefficient, P_L is the laser power, Φ_e is the laser diameter, x_S, and y_S are the horizontal positions of the laser beam center.

2.2. Numerical simulation setup

To investigate and simulate the complex physical phenomena such as heat transfer and molten metal flow in SLM process, a powder-scale computational fluid dynamics modelling was performed using simulation software FLOW-3D/FLOW-Weld version 2.3.4.6. A computational domain of this simulation is 0.6 mm × 1.4 mm x 0.25 mm as shown in Fig. 1. Three million computational mesh elements with the mesh size of 4.5 μm were utilized to the entire of simulation domain. The space region above the metal powder layer was set as atmospheric pressure and room temperature. Material used as the metal powder with different sizes of 19–43 μm and solid substrate is AISI H13 steel. A computational domain of this simulation was 0.6 mm × 1.4 mm x 0.25 mm as shown in Fig. 1. The space region above the metal powder layer was set as atmospheric pressure and room temperature of 298 K. Material used as the metal powder, with particle sizes of 19–43 μm, and solid substrate was AISI H13 steel. Material properties used in this simulation include solidus temperature of 1588 (K), liquidus temperature of 1727 (K), surface tension of 1.7 (kg/s^2), and surface tension coefficient of −0.00043 (kg/s^2K) respectively. In addition, latent heat of fusion and latent heat of evaporation of AISI H13 steel are 2.5×10^5 (J/kg) and 7.34×10^6 (J/kg) [14,15]. The thermal physical properties with temperature dependence including density, specific heat, and thermal conductivity of AISI H13 steel used in the simulation is tabulated in Table 1.

3. Mesh convergence analysis

In order to acquire a reliability of numerical model, mesh convergence analysis was investigated to determine the appropriate mesh size for this study. The mesh sizes used in the investigation were 3, 3.5, 4, 4.5, 5, 8, and 10 μm. Each mesh size provided total mesh elements of 9, 6, 4, 3, 2, 0.45 and 0.2 million respectively. The workstation intel® Xeon® 28 cores E5-2683 V3 CPU with 112 GB RAM was used for this study. The convergence of mesh size was performed by considering the melt track width. As presented in Table 2, it can be noted that the melt track width converged with mesh sizes smaller than 4.5 μm, while the solving time increased. Therefore, from consideration of convergence and solving time, the mesh size of 4.5 μm was selected for the simulation in this study.

4. Results and discussions

4.1. Thermal behavior and molten metal flow characteristic

Temperature distribution in the simulation domain during SLM process with laser power of 200 W and scanning speed of 1000 mm/s at different times is shown in Fig. 2 (a) as color contour plot. At 50 μs, the model depicted the temperature distribution with a round shape. The red color area appearing around the irradiated spot showed temperature greater than or equal to 1727 K. At 500 μs, the temperature distribution changed from round shape to a comet-like shape which its tail pointed opposite to the laser heat source moving direction. The temperature was decreased from the center to the edge of melt pool boundary. As laser heat source moving along the scanning direction for 700 and 1000 μm, the comet-shape area of the temperature distribution expanded due to the heat accumulation in metal powder and solid substrate. Furthermore, scanning track or melt track formation evolution is shown in Fig. 2 (b). The temperature and velocity flow field are presented as color contour and vector plot, respectively. At the beginning of SLM process, Fig. 2 b(v), the laser heat source irradiation resulted the round shape melt pool which the orange color region was depressed by recoil pressure. The vectors showed molten metal on the melt pool surface flowing from the center toward the edge. Subsequently, the melt pool transformed from round to elliptical shape while the laser heat source moving forward on the scanning direction as

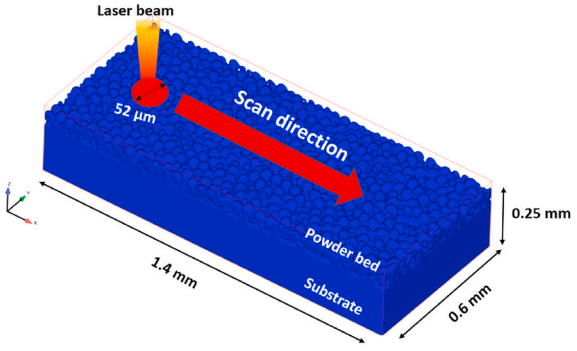

Fig. 1. The schematic of simulation domain.

Table 1
Thermal physical properties with temperature dependent of AISI H13 steel [17–20].

Temperature (K)	298	373	773	1073	1373	1473	1673	1873
Density (kg/m^3)	7650	7650	7640	7600	7550	7100	7000	7000
Specific heat (J/kgK)	447	453	519	573	625	642	677	708
Thermal conductivity (W/mK)	29.50	30.30	35.39	43.90	45.59	50.70	21.98	24.06

Table 2
Mesh convergence analysis.

Mesh sizes (μm)	10.0	8.0	5.0	4.5	4.0	3.5	3
No. mesh elements (million)	0.2	0.45	2	3	4	6	9
Melt track width (μm)	100.0	103.0	105.2	106.0	106.2	106.4	106.5
Solving time (min)	21	35	240	300	480	780	1500

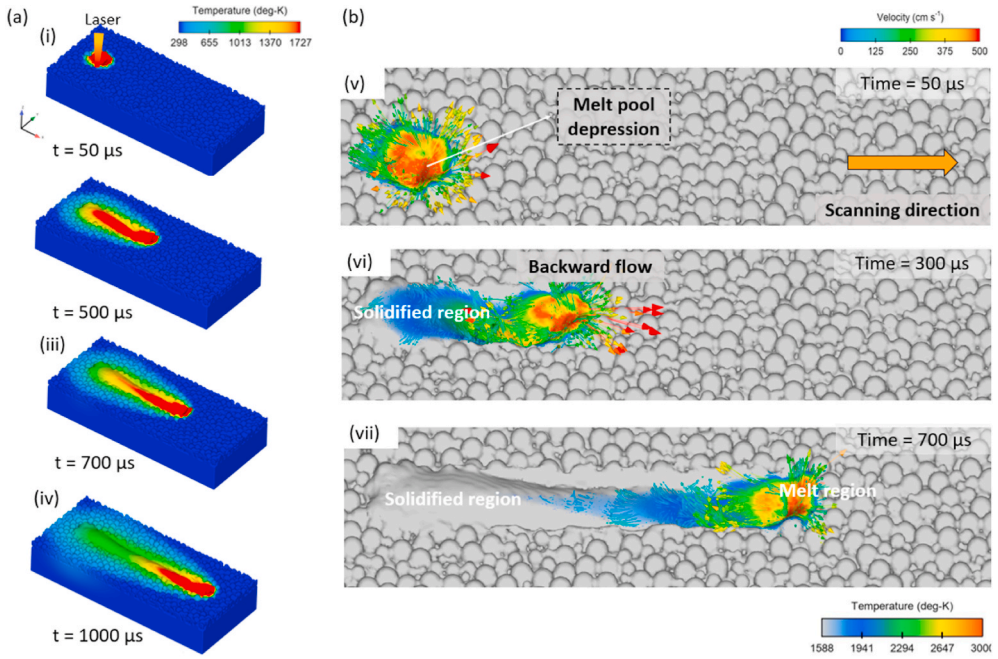

Fig. 2. (a) Temperature distribution on metal powder bed with laser power of 200 W and scanning speed of 1000 mm/s with different time and (b) Scanning track formation evolution during SLM process.

observed in Fig. 2 b(vi). The molten metal rearward flowed from the center to the tail of the melt pool due to Marangoni effect of the different surface tension. After the heat source move further along the scanning track, temperature of the tail of melt pool gradually reduced, and then the solidified track or scanning track was formed below the solidus temperature of 1588 K. Due to the influence of heat dissipation, Marangoni convection, and heat accumulation, the solidification from the edge to the center of melt pool formed the tear-drop shaped scanning track as illustrated in Fig. 2 b(vii).

Temperature evolution during SLM process monitored by a probe setting at the middle of powder bed is exhibited in Fig. 3. At 300 μs, the probe still showed room temperature because laser heat source did not pass it. The temperature rose rapidly while the laser heat source passing the probe, and then plummeted to room temperature as there was no contact between the probe and the molten metal due to melt pool depression. After the laser heat source passed over the probe, surface tension gradient and Marangoni effect caused backward flow and raised the molten metal up to contact the probe showing temperature above the solidus temperature again. Subsequently, the temperature started to decline to the room temperature in solidification stage.

The evolution of melt pool at x = 0.5 mm section view during the laser heat source passing through is displayed in Fig. 4. The molten region and the velocity flow field that occur during molten pool evolution are presented by red color and arrows. At 250 μs while the edge of laser spot just reached the observed section plane, metal powder began to melt, and transfer the heat to the substrate below. At 300 μs, the center of laser beam moved just above the observed section plane and irradiated the metal powder fully melted. Recoil pressure on the surface of molten metal depressed downward flow as indicated by direction arrows, then a keyhole was formed as seen at 350 μs. As laser heat source moved away from the observed section plane, recoil pressure was released therefore the molten

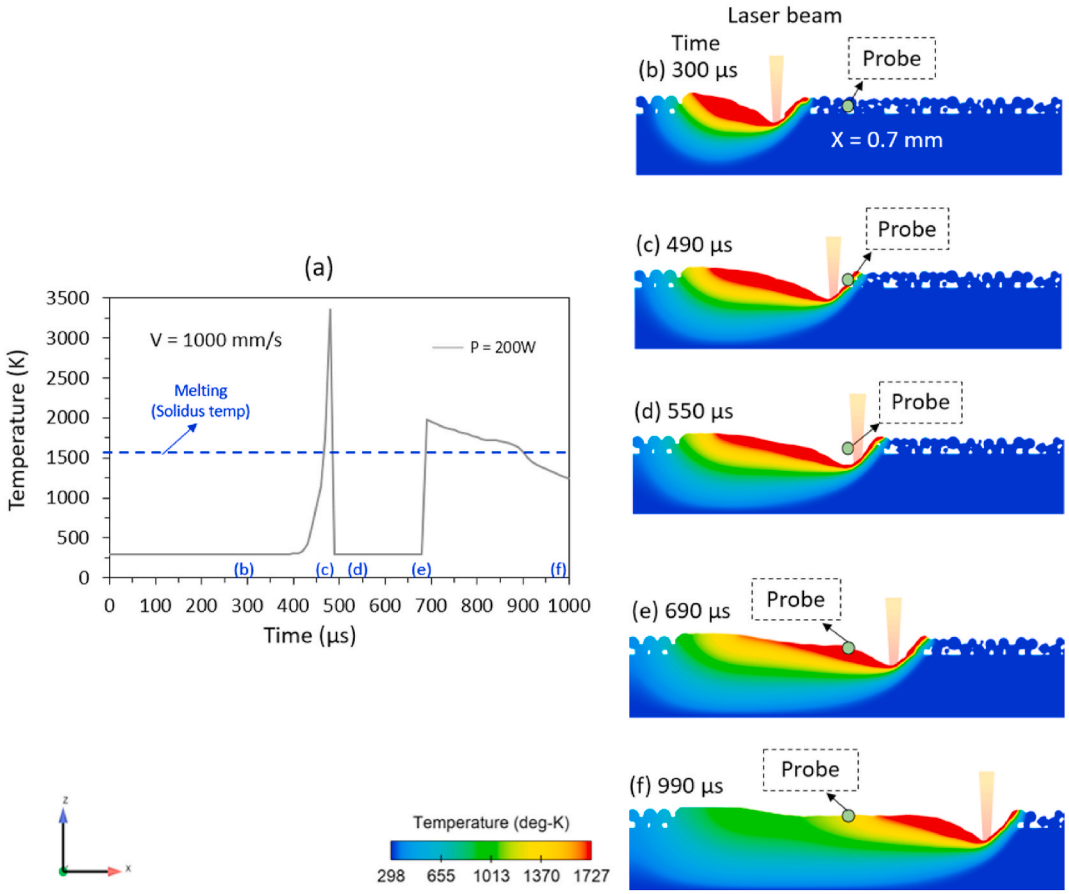

Fig. 3. Temperature evolution observed at the middle point of powder bed during SLM process with laser power of 200 W and scanning speed of 1000 mm/s.

metal changed to flow upward filling the keyhole because of the gravity force. Finally, the melt pool underwent cooling and solidification which induced the Marangoni effect to generate convex scanning track surface as shown in Fig. 4 (f)–(i).

4.2. The evolution of molten pool with varied processing parameters

A good understanding of the evolution of molten pool with varying processing parameters in SLM process has a great significance to control the quality of final build parts. Fig. 5 shows the evolution of melt pool with different process parameters at monitoring section view x = 0.5 mm. The temperature distribution that occurs during the molten pool formation and evolution is displayed by color bar of temperature in the right bottom corner of Fig. 5. The direction and magnitude of velocity flow filed are presented by direction arrows and the color bar in the left bottom corner of Fig. 5 (a1) - (c4). For this research, three case studies with laser power and scanning speed of 150 W and 1000 mm/s, 200 W and 1000 mm/s, 200 W and 1200 mm/s are selected to present the effect of laser power and scanning speed on molten pool formation and evolution. The initial state of the molten pool evolution of three different cases are shown in Fig. 5 (a1), (b1), and (c1). With laser power and scanning speed of 150 W and 1000 mm/s, the metal powders, which is spread on the solid substrate, are not melted due to low heat energy and heat transfer from the laser heat source (a1). While at the combination of 200 W and 1000 mm/s, the metal powder started to melt and begins to transfer heat to the solid substrate (b1). Whereas, the complete melting between metal powder and solid substrate can be observed with the combination of 200 W and 1200 mm/s as the moving laser beam arrives at monitoring plane as depicted in Fig. 5 (c1). As time progresses, the formation of molten pool with different process parameters are presented in (a2), (b2), and (c2). It can be noted that the melting stage of molten pool in conduction mode is generated with the combination 150 W and 1000 mm/s, and 200 W and 1200 mm/s due to low heat energy from laser heat source to metal powder as shown in Fig. 5 (a2), (c2). The molten pool in conduction mode typically provided the wide and shallow molten pool shapes. On the other hand, when the similar the scanning speed of 1000 mm/s, but the laser power was increased from 150 W to 200 W, the molten pool in transition mode, which effects from the recoil pressure and Marangoni flow resulting depression of molten pool, was formed due to high thermal energy from laser beam and more heat transfer between the metal powder and the solid substrate as shown in Fig. 5 (b2). Furthermore, the solidification and cooling stages of molten pool can take place after the laser source moves away from monitoring section as seen at 450 μs and 650 μs. As shown in Fig. 5 (a3), (b3), (c3), the flow of molten metal in solidification stage of all

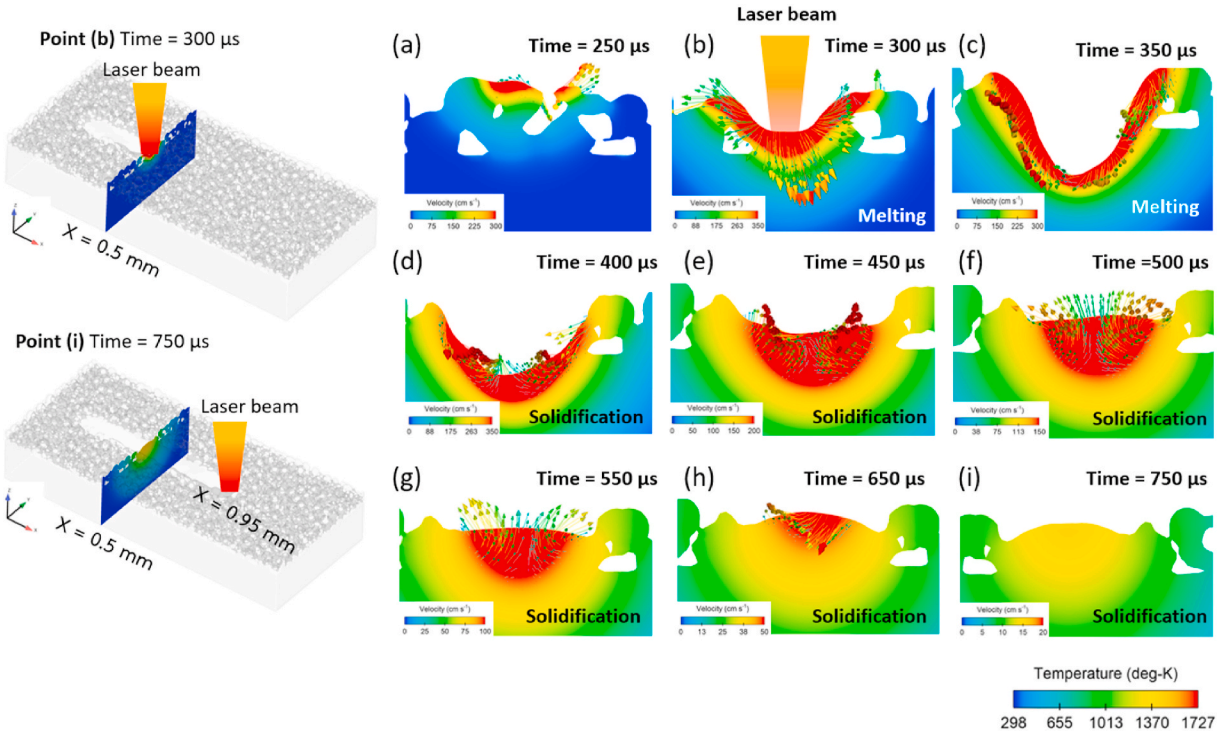

Fig. 4. Melt pool evolution at x = 0.5 mm section view during SLM process.

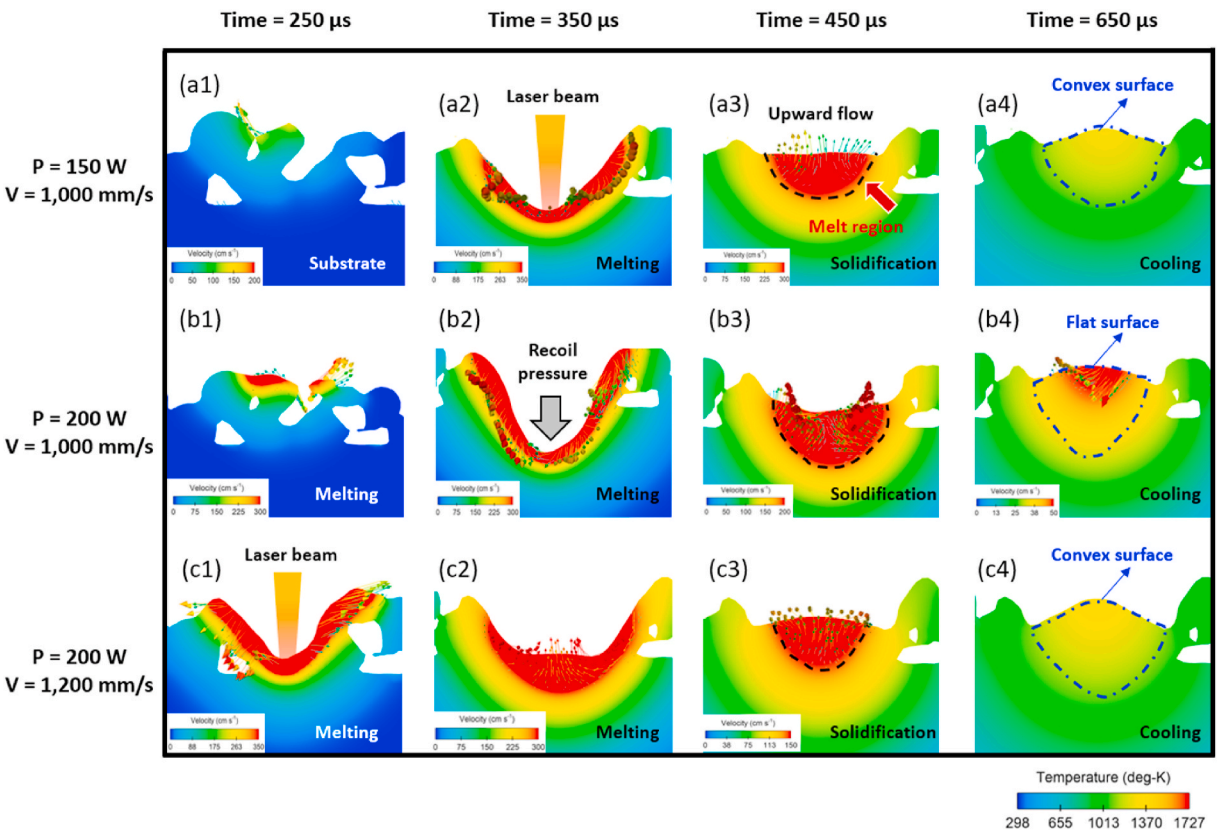

Fig. 5. The evolution of melt pool with different process parameters at monitoring section view x = 0.5 mm.

case studies alter from below direction to above direction to fill the gap because of the absence of recoil pressure. At 650 μs, the final shape and cooling stage of molten pool are illustrated in Fig. 5 (a4), (b4), (c4). The molten pool that formed convex shape can be generated by the Marangoni effect induced from surface tension gradient. At the laser power of 200 W and scanning speed of 1000 mm/s, it can be obviously seen that the molten metal still takes place at the above of molten pool as presented in red color region in Fig. 5 (b4). This is due to a large heat accumulation and low cooling rate of molten pool. In contrast, with the combination 150 W and 1000 mm/s, and 200 W and 1200 mm/s, the melt pool with solid state was completely formed. Moreover, it can also be seen that the final shape and surface morphology of molten pool for each condition are distinctive. The final shape of molten pool is marked with blue dash-dotted lines. As shown in Fig. 5 (a4) and (c4), the molten pool with laser power and scanning speed of 150 W and 1000 mm/s, and 200 W and 1200 mm/s showed the irregular shape, convex surface morphology and shallow of penetration depth. On the other hand, the uniform tear-drop shape molten pool with flat top surface and high penetration in the substrate can be observed when the laser power and scanning speed of 200 W and 1000 mm/s are applied as illustrated in Fig. 5 (b4).

4.3. *Influence of SLM process parameters on scanning track formation*

The temperature distribution during the SLM process under different laser power and scanning speed is shown in Fig. 6. The simulation results pointed out that the temperature distribution region with laser power of 250 W and scanning speed of 1000 mm/s can expand more than that of laser power of 200 W and scanning speed of 1500 mm/s due to the combination of thermal accumulation of metal powder and a longer time to interact between the laser heat source and the powder bed. These phenomena influence thermal stress, distortion, and cracking of final build parts.

Fig. 7 demonstrates the temperature evolution under different laser power and scanning speed which was monitored by probe A setting at the middle of powder bed and probe B setting 0.8 mm below the probe A in the substrate. The highest point of temperature took place when the laser heat source passed the probe. The temperature peak of higher laser power was higher than that of lower laser power as observed in Fig. 7 (b) and (c). For instance, at the probe A, the peak temperature of 250 W, 200 W and 150 W with the same scanning speed were around 4698 K, 3355 K, and 1963 K, respectively. In contrast, when increasing the scanning speed, the temperature peak decreased due to shorter time that metal powder absorbed the laser energy as observed in Fig. 7 (d) and (e). For example, at the probe B, the peak temperature of 1000 mm/s, 1200 mm/s, and 1500 mm/s with the same laser power were approximately 1545 K, 1094 K, and 898 K, respectively. The physical phenomena have an influence on microstructure evolution and mechanical properties of final parts.

Fig. 8 exhibits the cross-sections of scanning track under different laser power and scanning speed from numerical modelling. Dimensions of the scanning track width, w, depth, d, and height, h, as defined in Fig. 8 (b), d/w ratio, and h/w ratio were illustrated in Table 3. The numerical simulation results revealed that the high penetration and uniform tear-drop shape scanning tracks, defining as flat top surface and sufficient penetration of melt track, took place with the laser power and scanning speed of 200 W and 1000 mm/s, 250 W and 1000 mm/s, and 250 W and 1200 mm/s due to high heat input from laser energy to metal powder bed. The criteria of uniform tear-drop shape in this study were d/w ratio $\geq$0.7 and h/w ratio $\leq$0.2. On the contrary, the scanning tracks with laser power and scanning speed of 150 W and 1000 mm/s, 150 W and 1200 mm/s, 150 W and 1500 mm/s, 200 W and 1200 mm/s, 200 W and 1500 mm/s, and 250 W and 1500 mm/s provided the irregular shape and shallow of penetration depth scanning track due to

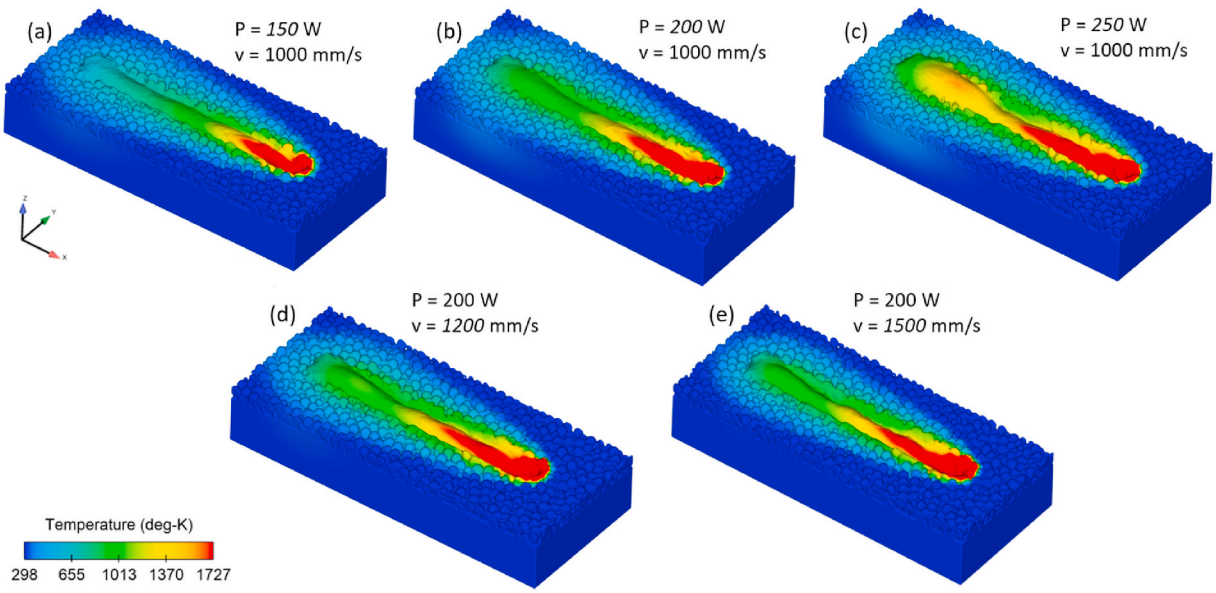

Fig. 6. Temperature distribution during the SLM process with different laser power and scanning speed.

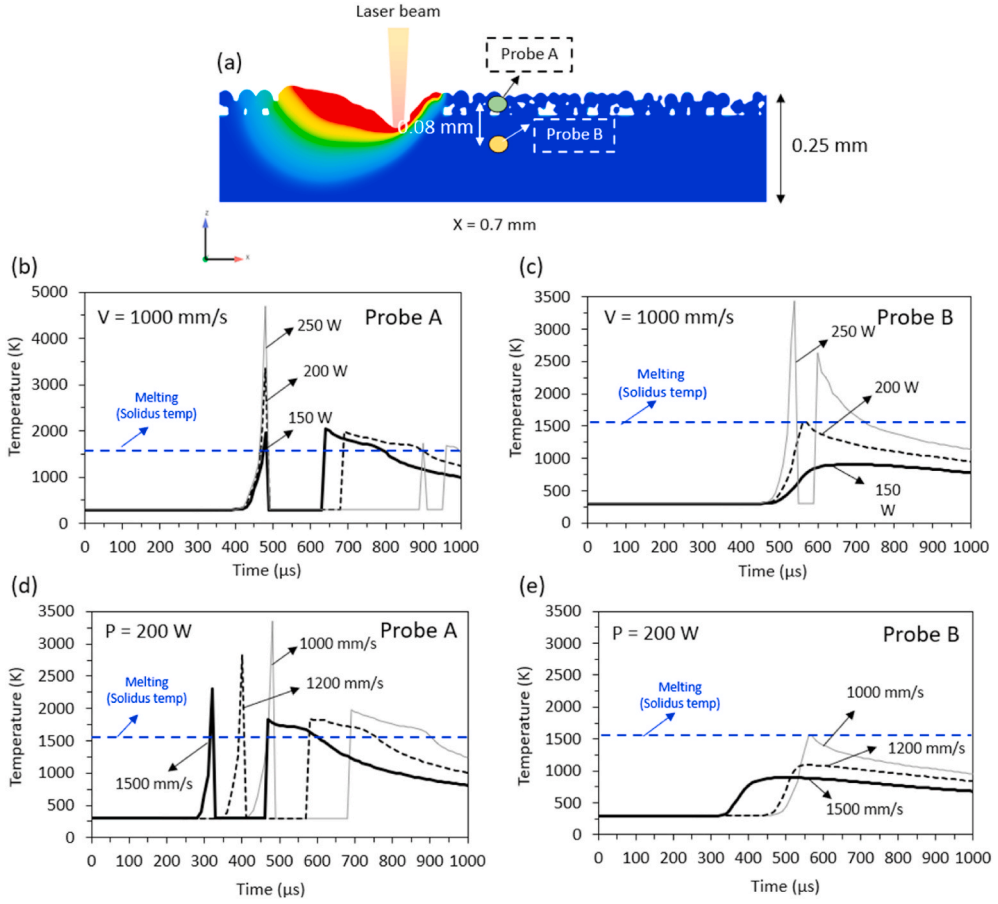

Fig. 7. Influence of laser power and scanning speed on the temperature evolution.

insufficient energy heat input. It can be noted that the scanning track width and depth of all scanning speeds increased with increasing laser power, i.e. increased around 4–10 μm and 14–22 μm, respectively, with the increase in laser power of 50 W. Moreover, it was found that with higher scanning speed, the laser power had greater effect to the track width variation than with lower scanning speed. For example, at the scanning speed of 1500 mm/s, the track width difference between laser power of 200 W and 250 W was around 10 μm, while it was around 4 μm at the scanning speed of 1000 mm/s. Likewise, the scanning track width and depth decreased around 1–4 μm and 3–6 μm, respectively, per increasing in scanning speed of 100 mm/s for all cases of different laser power. The width and depth of scanning track are significant factors to determine the hatch spacing and overlap rate of multi tracks scanning to achieve the full dense parts.

4.4. Numerical simulation validation

The numerical modelling result in the current study was validated with the experimental result from Y. Ch. Wu et al. [14]. Fig. 9 shows the comparison of molten pool region between the simulation result obtained from this study (a) and the experimental measurement from Y. Ch. Wu et al. (b). The contour plot of numerical modelling represents the melt and unmelt region in red and blue color respectively. The simulation and the experimental results were in reasonable agreement with minor differences of molten pool width and depth. Consequently, it was assured that the numerical model in this present study can be further utilized to investigate and simulate the influence of SLM parameters on thermal behavior, molten metal flow characteristic, and single scanning track formation.

5. Conclusions

In the present research, a powder-scale CFD model was carried out to examine the thermal behavior and molten metal flow characteristic, analyze the influence of laser power and scanning speed on scanning track formation, and provide an insight understanding on the complex physics in SLM process of AISI H13 tool steel. The results reveal that the CFD model can be utilized to describe the mechanism of complex physical phenomena in the SLM process such as heat transfer and molten metal flow characteristics. The molten metal can flow backward from the laser hot spot to the tail of molten pool because of the difference between surface tension at

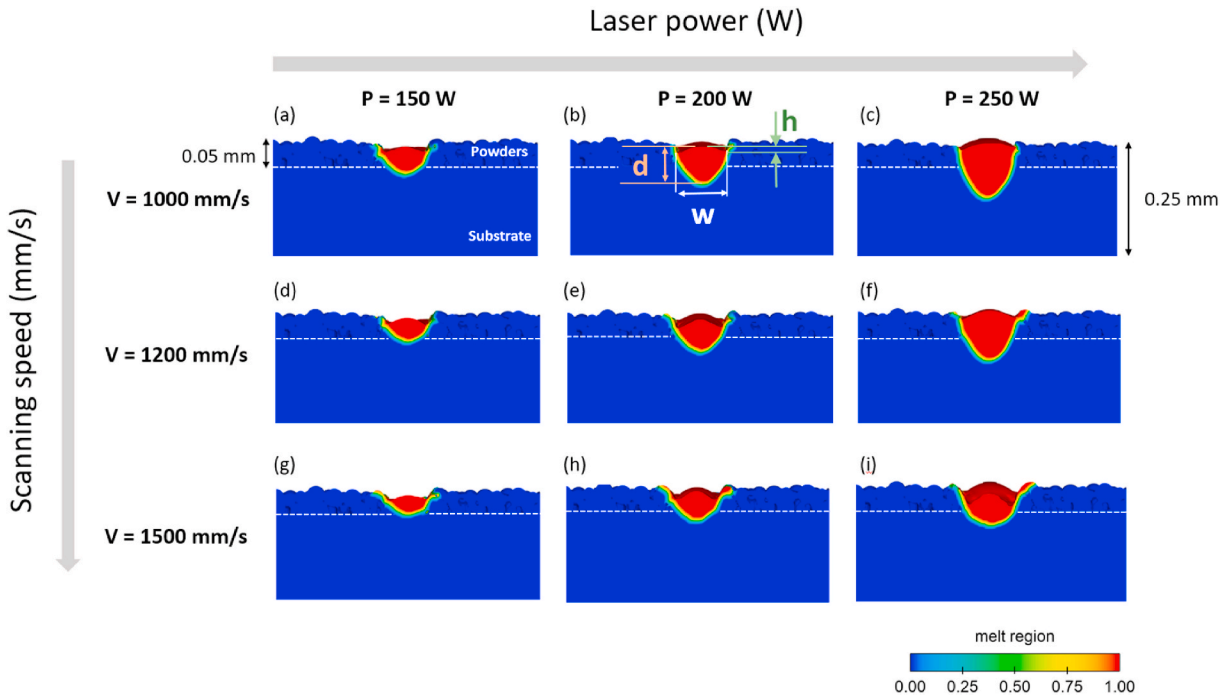

Fig. 8. Cross-sections of scanning track under different laser power and scanning speed.

Table 3
The scanning track width, depth, height, d/w ratio, and h/w ratio under different laser power and scanning speed.

P (W)	v (mm/s)	w (μm)	d (μm)	h (μm)	d/w ratio	h/w ratio	Uniform tear-drop shape
150	1000	97	59	10	0.61	0.10	No
200	1000	106	81	16	0.76	0.15	Yes
250	1000	110	95	11	0.86	0.10	Yes
150	1200	89	50	15	0.56	0.17	No
200	1200	98	70	19	0.71	0.20	Yes
250	1200	104	87	17	0.84	0.16	No
150	1500	83	42	15	0.50	0.18	No
200	1500	91	61	24	0.67	0.26	No
250	1500	101	77	26	0.76	0.25	No

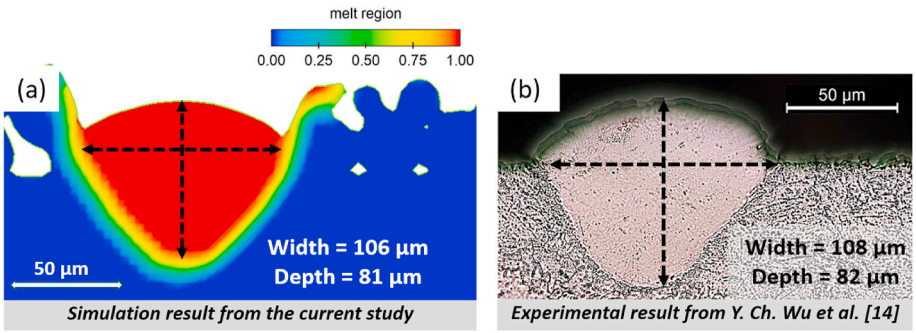

Fig. 9. The comparison of molten pool region between simulation result obtained from the current study (a) and the experimental result measurement from Y. Ch. Wu et al. (b).

the hot spot and at the tail. Scanning track with uniform tear-drop shape and high penetration can be formed with laser power and scanning speed of 200 W and 1000 mm/s, 250 W and 1000 mm/s, and 250 W and 1200 mm/s. Furthermore, it was also found that the scanning track width and depth increased around 4–10 μm and 14–22 μm, respectively, with the increase in laser power of 50 W, and

decreased around 1–4 μm and 3–6 μm, respectively, per increasing in scanning speed of 100 mm/s.

CRediT authorship contribution statement

Patiparn Ninpetch: Conceptualization, Methodology, Software, Validation, Investigation, Visualization, Writing - original draft, Writing - review & editing. **Pruet Kowitwarangkul:** Supervision, Project administration, Conceptualization, Formal analysis, Investigation, Visualization, Writing - original draft, Writing - review & editing, Funding acquisition. **Sitthipong Mahathanabodee:** Investigation, Writing - original draft, Writing - review & editing. **Prasert Chalermkarnnon:** Methodology, Investigation, Writing - original draft, Writing - review & editing. **Phadungsak Rattanadecho:** Supervision, Formal analysis, Writing - original draft.

Declaration of competing interest

The authors declare that they have no known competing financial interests or personal relationships that could have appeared to influence the work reported in this paper.

Acknowledgement

This research was funded by the Thailand Science Research and Innovation (TSRI) Contract no. MRG6180164, and the Thailand Government Budget Grant, King Mongkut's University of Technology North Bangkok, Contract no. KMUTNB-63-KNOW-023, and Thailand Graduate Institute of Science and Technology (TGIST), National Science and Technology Development Agency (NSTDA) Contract no. SCA–CO–2562-9649-TH. The author would also like to thank software license support from Flow Science, Inc, Flow Science Japan and Design Through Acceleration Co., Ltd.

References

[1] Q. Jia, D. Gu, Selective laser melting additive manufacturing of Inconel 718 superalloy parts: densification, microstructure, and properties, J. Alloys Compd. 585 (2014) 713–721, https://doi.org/10.1016/j.jallcom.2013.09.171.
[2] M. Xia, D. Gu, G. Yu, D. Dai, H. Chen, Q. Shi, Influence of hatch spacing on heat and mass transfer, thermodynamics, and laser processability during additive manufacturing of Inconel 718 alloy, Int. J. Mach. 109 (2016) 147–157, https://doi.org/10.1016/j.ijmachtools.2016.07.010.
[3] M. Bayat, S. Mohanty, J.H. Hattel, Multiphysics modelling of lack-of-fusion voids formation and evolution in IN718 made by multi-track/multi-layer L-PBF, Int. J. Heat Mass Tran. 139 (2019) 95–144, https://doi.org/10.1016/j.ijheatmasstransfer.2019.05.003.
[4] D.L. Bourell, M.C. Leu, J.J. Beaman, D.W. Rosen, A Brief History of Additive Manufacturing and the 2009 Roadmap for Additive Manufacturing: Looking Back and Looking Ahead, US – TURKEY Workshop on Rapid Technologies, 2009.
[5] T. Wohlers, Additive Manufacturing State of the Industry, Wohlers report, 2010, pp. 1–26.
[6] Y.S. Lee, W. Zhang, Mesoscopic simulation of heat transfer and fluid flow in laser powder bed additive manufacturing, in: Proc. Of International Solid Free Form Fabrication Symposium, 2015, pp. 1154–1165. Austin, TX, USA.
[7] P. Ninpetch, P. Kowitwarangkul, S. Mahathanabodee, P. Chalermkaranon, P. Rattanadecho, A review of computer simulations of metal 3D printing, AIP Conf. Proc. 2279 (2020), 050002, https://doi.org/10.1063/5.0022974.
[8] W. Yan, Y. Qian, W. Ge, S. Lin, W.K. Liu, F. Lin, G.J. Wagner, Meso-scale modeling of multiple-layer fabrication process in selective electron beam melting: inter-layer/track voids formation, Mater. Des. 141 (2018) 210–219, https://doi.org/10.1016/j.matdes.2017.12.031.
[9] Y. Xiang, Sh Zhang, Zh Wei, J. Li, P. Wei, Zh Chen, Li Yang, Li Jiang, Forming and defect analysis for single track scanning in selective laser melting of Ti6Al4V, Appl. Phys. A 124 (2018) 1–12, https://doi.org/10.1007/s00339-018-2056-9.
[10] B. Cheng, L. Loeber, H. Willeck, U. Hartel, Ch Tuffile, Computational investigation of melt pool process dynamics, and pore formation in laser powder bed fusion, J. Mater. Eng. Perform. 28 (2019) 1–14, https://doi.org/10.1007/s11665-019-04435-y.
[11] L. Cao, Numerical simulation of the impact of laying powder on selective laser melting single-pass formation, Int. J. Heat Mass Tran. 141 (2019) 1036–1048, https://doi.org/10.1016/j.ijheatmasstransfer.2019.07.053.
[12] Y. Li, D. Gu, Thermal behavior during selective laser melting of commercially pure titanium powder: numerical simulation and experimental study, Addit. Manuf. 1 (2014), https://doi.org/10.1016/j.addma.2014.09.001.
[13] P. Ninpetch, P. Kowitwarangkul, S. Mahathanabodee, R. Tongsri, P. Rattanadecho, Thermal and melting track simulations of laser powder bed fusion (L-PBF), IOP Conf. Ser. Mater. Sci. Eng. 526 (2019) 1–4, https://doi.org/10.1088/1757-899X/526/1/012030.
[14] Y. Ch Wu, Ch H. San, Ch H. Chang, H.J. Lin, R. Marwan, S. Baba, W.S. Hwang, Numerical modeling of melt-pool behavior in selective laser melting with random powder distribution and experimental validation, J. Mater. 254 (2018) 72–78, https://doi.org/10.1016/j.jmatprotec.2017.11.032.
[15] B. Cheng, X. Li, Ch Tuffile, A. Ilin, H. Willeck, U. Hartel, Multi-physics modeling of single-track scanning in selective laser melting: powder compaction effect, in: Proc. 29th International Solid Free Form Fabrication Symposium, 2018, pp. 1887–1902. Austin, TX, USA.
[16] Y. Ch Wu, W.S. Hwang, Ch H. San, Ch H. Chang, H.J. Lin, Parametric study of surface morphology for selective laser melting on Ti6Al4V powder bed with numerical and experimental methods, Int. J. Material Form. 11 (2018) 807–813, https://doi.org/10.1007/s12289-017-1391-2.
[17] Y. Woo, T. Hwang, I. Oh, D. Seo, Y. Moon, Analysis on selective laser melting of WC-reinforced H13 steel composite powder by finite element method, Adv. Mech. Eng. 11 (2019) 1–11, https://doi.org/10.1177/1687814018822200.
[18] P. Farahmand, P. Balu, F. Kong, R. Kovacevic, Investigation of Thermal Cycle and Hardness Distribution in the Laser Cladding of AISI H13 Tool Steel Produced by a High-Power Direct Diode Laser, Proc. of ASME International Mechanical Engineering Congress & Exposition, San Diego, California, USA, 2013, pp. 1–12.
[19] Q. Tang, P. Chen, J. Chen, Y. Chen. H. Chen, Numerical simulation of selective laser melting temperature conduction behavior of H13 steel in different models. Optik 201 (Article in press).
[20] AISI H13/1.2344/SKD61. http://www.round-bars.com/products/H13-SKD61-hot-work-tool-steel/, 2020. (Accessed 10 June 2020).